Photovoltaic and Amplified Spontaneous Emission Studies of High-Quality Formamidinium Lead Bromide Perovskite Films

Neha Arora, M. Ibrahim Dar,* Mahmoud Hezam, Wolfgang Tress, Gwénolé Jacopin, Thomas Moehl, Peng Gao, Abdulah Saleh Aldwayyan, Benoit Deveaud, Michael Grätzel, and Mohammad Khaja Nazeeruddin*

This study demonstrates the formation of extremely smooth and uniform formamidinium lead bromide ($CH(NH_2)_2PbBr_3$ = $FAPbBr_3$) films using an optimum mixture of dimethyl sulfoxide and *N,N*-dimethylformamide solvents. Surface morphology and phase purity of the $FAPbBr_3$ films are thoroughly examined by field emission scanning electron microscopy and powder X-ray diffraction, respectively. To unravel the photophysical properties of these films, systematic investigation based on time-integrated and time-dependent photoluminescence studies are carried out which, respectively, bring out relatively lower nonradiative recombination rates and long lasting photogenerated charge carriers in $FAPbBr_3$ perovskite films. The devices based on FTO/TiO_2/$FAPbBr_3$/spiro-OMeTAD/Au show highly reproducible open-circuit voltage (V_{oc}) of 1.42 V, a record for $FAPbBr_3$-based perovskite solar cells. V_{oc} as a function of illumination intensity indicates that the contacts are very selective and higher V_{oc} values are expected to be achieved when the quality of the $FAPbBr_3$ film is further improved. Overall, the devices based on these films reveal appreciable power conversion efficiency of 7% under standard illumination conditions with negligible hysteresis. Finally, the amplified spontaneous emission (ASE) behavior explored in a cavity-free configuration for $FAPbBr_3$ perovskite films shows a sharp ASE threshold at a fluence of 190 µJ cm^{-2} with high quantum efficiency further confirming the high quality of the films.

1. Introduction

The growing demand for renewable energy has brought solar cells to the forefront as a potential energy harvester. Consequently, organic–inorganic metal halide perovskite solar cells have garnered profound research interest in recent years as next-generation photovoltaics.[1] This importance stems largely from their exceptional charge carrier mobilities, and optical and electronic properties that are tunable by varying the chemical composition.[2,3] Recently, perovskite-based solar cells have demonstrated an impressive power conversion efficiency (PCE) of over 20%.[4] In most of the practical applications of solar cells, besides the importance of short-circuit current density, high open-circuit voltage (V_{oc}) is an indispensable parameter to attain both high power conversion efficiency with reduced series resistance losses and to drive electrochemical reactions including water-splitting reactions and CO_2 reduction.[5,6] In principle, a high open-circuit voltage in a perovskite solar cell can be attained by aligning the energy levels of absorber and charge extraction layers.[7] Despite having enticing benefit of higher bandgap for pure bromide-based perovskite material

Dr. N. Arora, Dr. M. I. Dar, Dr. P. Gao,
Prof. M. K. Nazeeruddin
Group for Molecular Engineering of Functional Materials
Institute of Chemical Sciences and Engineering
École Polytechnique Fédérale de Lausanne
Lausanne CH-1015, Switzerland
E-mail: ibrahim.dar@epfl.ch; mdkhaja.nazeeruddin@epfl.ch
Dr. M. I. Dar, Dr. W. Tress, Dr. T. Moehl,
Prof. M. Grätzel
Laboratory of Photonics and Interfaces
Institute of Chemical Sciences and Engineering
École Polytechnique Fédérale de Lausanne
Lausanne CH-1015, Switzerland

M. Hezam
King Abdullah Institute for Nanotechnology
King Saud University
Riyadh 11451, Saudi Arabia
M. Hezam, Dr. G. Jacopin, Prof. B. Deveaud
Laboratory of Quantum Optoelectronics
Institute of Physics
École Polytechnique Fédérale de Lausanne
Lausanne CH-1015, Switzerland
Prof. A. S. Aldwayyan
Physics and Astronomy Dept, Photonics Lab
College of Science
King Saud University
Riyadh 11451, Saudi Arabia

ADVANCED
FUNCTIONAL
MATERIALS
www.afm-journal.de

Materials Views
www.MaterialsViews.com

FULL PAPER

which indeed can also be used as a top cell in tandem solar cells,[8] much of the research mainly focused on pure iodide ($CH_3NH_3PbI_3$), mixed halide ($CH_3NH_3PbI_{3-x}Br_x$) or double-mixed (($CH(NH_2)_2PbI_3)_{1-x}(CH_3NH_3PbBr_3)_x$) perovskites.[4] Nevertheless, promising studies on efficient methylammonium lead bromide ($CH_3NH_3PbBr_3$)-based device architecture showing enhanced photovoltage in comparison to pure iodide-based perovskite have been documented. Kojima et al. reported on employing $CH_3NH_3PbBr_3$ as visible-light sensitizers in photoelectrochemical cells exhibiting a promising photovoltage of 0.96 V with a power conversion efficiency of 3.1%.[9] Later on, Edri et al. demonstrated a high V_{oc} of 1.3 V based on alumina\$CH_3NH_3PbBr_3$\$N,N'$-dialkyl perylenediimide (PDI) solar cell structure, however the efficiency of the devices was quite low (< 1%).[10] Recently, by controlling the crystallization process of $CH_3NH_3PbBr_3$ as well as by tailoring the highest occupied molecular orbital (HOMO) levels of different hole-transporting materials (HTMs), a V_{oc} of 1.51 V has been reported.[11]

So far, most of the studies on bromide perovskites are devoted to $CH_3NH_3PbBr_3$, however, the focus of this work constitutes formamidinium lead bromide ($CH(NH_2)_2PbBr_3$ = FAPbBr$_3$) perovskite which has been studied scantly. Earlier, Hanusch et al. described the fabrication of planar heterojunction FAPbBr$_3$ perovskite solar cells with efficiency of over 6%,[12] however, the device exhibited severe hysteresis which leads to an overestimation of power conversion efficiency. Mostly the presence of mesoporous TiO_2 scaffold has proven to be advantageous in reducing the scan speed dependent hysteresis observed in current–voltage ($J–V$) curves in perovskite solar cells.[13,14] Tuning the growth of perovskite structures has been one of the critical parameters to fabricate high-efficiency solar cells. To that end, we investigated the role of solvent on the growth and morphology of FAPbBr$_3$ perovskite films, which eventually led to the enhancement in the photovoltage to a remarkable extent. We fabricated FAPbBr$_3$ films employing the sequential deposition method involving a mixture of solvents, N,N-dimethylformamide and dimethyl sulfoxide(DMF+DMSO) for the PbBr$_2$ precursor solution. Employing spiro-OMeTAD as a hole-transporting material led us to fabricate FAPbBr$_3$ perovskite devices with a J_{sc} of 6.8 mA cm^{-2}, FF of 72%, and V_{oc} of 1.42 V resulting in an overall efficiency of 7.0%. It is to be noted that these devices exhibited negligible hysteresis. The impact of the solvent on structural, morphological, and various photophysical properties which dictate the photovoltaic performance of a device was explored by X-ray diffraction (XRD), field emission scanning electron microscopy (FESEM), UV–visible absorption, low temperature photoluminescence (PL), and charge carrier lifetime studies.

Additionally, amplified spontaneous emission (ASE) was recorded from the FAPbBr$_3$ perovskite films. Recently, there has been a report in which formamidinium lead bromide perovskite nanoparticles were incorporated into light-emitting electrochemical cells.[15] In the literature various studies have demonstrated the enormous potential of perovskite materials as optical gain mediums even with a cavity-free configuration.[16,17] The low nonradiative recombination rate, long diffusion length, and high mobility of charge carriers reported for perovskites even with high defect trap densities, are key factors for their unprecedented progress in photovoltaics.[18–20]

In addition to slow Auger recombination, the various possibilities of fabricating them in different cavity configurations make them suitable for an efficient semiconductor laser.[21–23] In this work, a sharp transition from spontaneous emission (SE) to ASE at a pump fluence of 190 μJ cm^{-2} per pulse was observed in FAPbBr$_3$ perovskite films which corresponds to an ASE threshold carrier density of ≈2.3 × 10^{18} cm^{-3}. Although ASE has been reported for both $CH_3NH_3PbI_3$ and $CH_3NH_3PbBr_3$ perovskites in different resonating and cavity-free configurations as well as in random networks of nanocrystals,[16,17,21–23] to the best of our knowledge, there has been no report till date demonstrating the light gain applications of such FAPbBr$_3$ perovskite films.

2. Results and Discussion

Two different FAPbBr$_3$ perovskite films were deposited using the sequential deposition approach. Typically, a solution of PbBr$_2$ (DMF) or PbBr$_2$ (DMF+DMSO) was spin casted onto a mesoporous TiO_2 scaffold. Subsequently the resulting films were converted into FAPbBr$_3$ perovskite films by dipping into isopropanol solution of formamidinium bromide ($CH(NH_2)_2Br$), which were labeled as **FA(1)** (obtained from PbBr$_2$ (DMF)) and **FA(2)** (obtained from PbBr$_2$ (DMF+DMSO)). (See the Experimental Section for more details.)

2.1. Structural and Morphological Characterization

To evaluate the crystallinity of **FA(1)** and **FA(2)** perovskite films, X-ray diffraction was performed at room temperature. The XRD patterns (Figure S1, Supporting Information) obtained from the films could be indexed to the cubic phase of FAPbBr$_3$ with a space group $Pm–3m$, which is consistent with previous reports.[12,15]

The morphology of lead bromide and FAPbBr$_3$ films was probed by FESEM. From SEM analysis, it is evident that coverage of the lead bromide films obtained from PbBr$_2$ (DMF) (**Figure 1**a) solution is relatively poor whereas the deposition of PbBr$_2$ (DMF+DMSO) solution led to the formation of a uniform lead bromide film (Figure 1b). Furthermore, top view SEM micrograph of **FA(1)** perovskite sample reveals the formation of an inhomogeneous film composed of aggregated FAPbBr$_3$ structures (Figure 1c). On the contrary, extremely uniform and continuous FAPbBr$_3$ films with full surface coverage were obtained in case of **FA(2)**, as shown in Figure 1d. From a marked difference in the surface morphology of lead bromide and FAPbBr$_3$ films for **FA(1)** and **FA(2)** samples, we establish that the nature of the solvent employed for PbBr$_2$ precursor solution can considerably improve the surface coverage of the films, which ostensibly could be beneficial for the fabrication of efficient devices.[13]

The device fabrication was completed by spin coating spiro-OMeTAD as the hole-transporting material on FAPbBr$_3$ perovskite layer, followed by thermal evaporation of a 70 nm thick gold layer as a back contact. The cross-section SEM micrograph of **FA(1)** (Figure 1e) shows the formation of a nonuniform FAPbBr$_3$ film of ≈500 nm thickness (including mesoporous TiO_2).
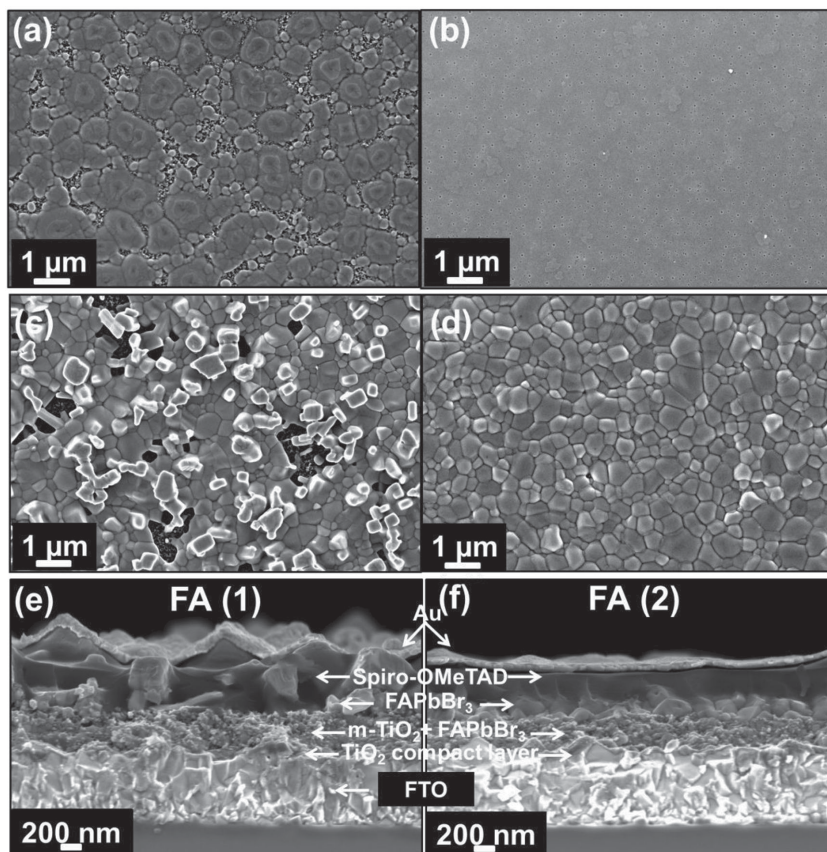
Figure 1. Scanning electron microscopy analysis. Top view of a) PbBr$_2$ (DMF), b) PbBr$_2$ (DMF+DMSO) films, c) **FA(1)**: FAPbBr$_3$ perovskite films prepared from PbBr$_2$ (DMF), d) **FA(2)**: FAPbBr$_3$ perovskite films prepared from PbBr$_2$ (DMF+DMSO). Cross-sectional SEM image of devices based on e) **FA(1)** and f) **FA(2)** films.

From the top view and cross-section SEM analysis, parasitic contacts between organic conductor (HTM) and the mesoporous TiO$_2$ layer as well as between pillared perovskite layer and top gold contact are observed. Expectedly, a mixture of solvents (DMF+DMSO) yields smoother and continuous FAPbBr$_3$ film with a uniform thickness of ≈300 nm, which is homogeneously covered with spiro-OMeTAD (Figure 1f).

From a detailed SEM analysis, we noticed that using a mixture of solvents (DMF+DMSO) for lead bromide precursor solution resulted in the formation of smoother films.[24–26] In addition to enhancement in solubility, mixed solvents possibly slow down the growth of lead halide structures during spin coating, yielding a uniform film (Figure 1b).[27] Low boiling solvent (DMF) evaporates rapidly and eventually enhances the loading (Figure 1e) whereas because of slower evaporation of high boiling solvent (DMSO), discontinuous and less loaded lead bromide and FAPbBr$_3$ films are formed, as evident from SEM and UV–visible spectrum (Figures S2,S3, Supporting Information). Smoother FAPbBr$_3$ film with an optimum thickness could warrant the fabrication of efficient perovskite solar cells. Therefore, to tailor the formation and loading of FAPbBr$_3$ structures, it became imperative to use a judicious ratio of low and high boiling solvents. As is known DMSO solvent has a tendency to form an adduct with lead iodide or it could

pronounce the amorphous nature of lead iodide films.[27,28] Using DMSO–lead iodide adduct, the fabrication of high-efficiency solar cells has been reported recently.[4,28] To understand the role of DMSO further, we recorded XRD patterns of **FA(1)** and **FA(2)** lead bromide films. Variation in the crystal structure of lead bromide films deposited from a single and a stoichiometric mixture of DMF+DMSO solvent (Figure S4, Supporting Information) was marginal which is in contrast to what has been observed in lead iodide films.[27]

2.2. Photovoltaic Properties of Formamidinium Perovskite Devices

Tailoring the growth and morphology of perovskite layer is one of the critical factors that led to the evolution of high-efficiency perovskite solar cells. Herein, we investigated the effect of morphology of FAPbBr$_3$ films on the performance of the resulting devices. The current–voltage curves of the **FA(1)** and **FA(2)** bromide perovskite devices are shown in **Figure 2** and the extracted photovoltaic parameters are summarized in **Table 1**. Under illumination of 100 mW cm^{-2}, the device based on **FA(1)** film (FAPbBr$_3$ film involving PbBr$_2$ (DMF) precursor solution), exhibits a high short-circuit current density (J_{sc}) of 7.1 mA cm^{-2}, a modest open-circuit voltage V_{oc} of 1.14 V, and a fill factor (FF) of 0.67, resulting in an overall power conversion efficiency (η) of 5.4% (Figure 2a). By contrast, **FA(2)** device exhibits similar short-circuit current density (J_{sc}) of 6.8 mA cm^{-2}, a record V_{oc} for formamidinium perovskite of 1.42 V, and a FF of 0.72, resulting in an overall conversion efficiency (η) of 7.0% (Figure 2b). Ostensibly, a higher J_{sc} value of 7.1 mA cm^{-2} obtained from **FA(1)** device could be due to the formation of thicker FAPbBr$_3$ films as evident from cross-sectional SEM analysis (Figure 1e). By changing the solvent from DMF to a stoichiometric mixture of DMF+DMSO solvents for the PbBr$_2$ precursor solution, V_{oc} increases significantly from 1.14 to 1.42 V which demonstrates that the morphology of the film has a considerable impact on the photovoltage.

2.2.1. Insight into the Origin of High V_{oc}

The V_{oc} > 1.4 V for **FA(2)** devices is extraordinarily high considering the contact materials FTO/TiO$_2$ and spiro-OMeTAD. Assuming that the work function of the FTO/TiO$_2$ is ≈ −4.0 to −4.2 eV and the HOMO in the doped spiro-OMeTAD at −5.4 eV and, thus, the work function close but smaller than this value, V_{oc} is larger than the built-in potential.[29] Therefore, the energetics of the contact materials do not merely define the V_{oc} as commonly reported in the literature.[30,31] Such a high V_{oc} is
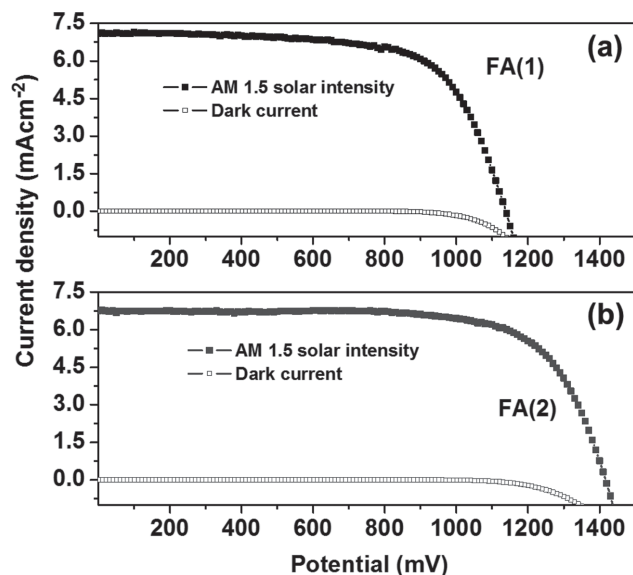
FULL PAPER

Figure 2. Photovoltaic performance of perovskite devices with spiro-OMeTAD as hole transporter recorded at a scan rate of 0.1 V s^{-1} under simulated AM1.5 100 mW cm^{-2} photon flux. a) **FA(1)**: FAPbBr$_3$ perovskite device prepared from PbBr$_2$ (DMF) and b) **FA(2)**: FAPbBr$_3$ perovskite device prepared from PbBr$_2$ (DMF+DMSO) solution.
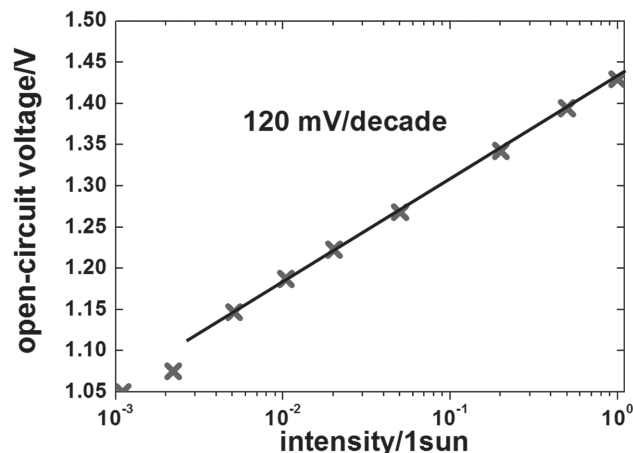

Figure 3. V_{oc} as a function of illumination intensity provided by white LEDs. A value of 1 sun delivers a short-circuit current close to the one at 100 mW cm^{-2} under simulated AM1.5.

only possible when free charge carrier generation occurs within the perovskite itself, i.e., interfaces to TiO$_2$ or spiro-OMeTAD are not required to split excitons. Additionally, recombination of photogenerated holes at FTO and electrons at spiro-OMeTAD has to be suppressed, i.e., contacts have to be selective. In that case, V_{oc} is determined by the equilibrium between carrier generation and recombination in the absorber itself, which defines the splitting of electron and hole quasi Fermi level. Given a sufficient diffusivity, charges are driven by diffusion towards their respective electrodes to generate photocurrent for voltages close to but smaller than V_{oc}.

To get a closer insight into the recombination mechanisms limiting V_{oc}, we measured V_{oc} as a function of illumination intensity.[32] The data shown in **Figure 3** with a slope of 120 mV/decade indicate that V_{oc} is determined by recombination via defects. Even at 1 sun, the slope is not decreased, which would be expected for limitations by surface recombination in case of a compensated built-in potential for large V_{oc}.[32] This indicates that the contacts are very selective and V_{oc} continues increasing for higher light intensities. In particular, spiro-OMeTAD does not seem to limit V_{oc} and higher V_{oc} values may be reached when the quality of the FAPbBr$_3$/TiO$_2$ film is further improved, i.e., the defect density reduced, while maintaining the contact materials. The high selectivity of the device structure is given by offsets in the valence band of TiO$_2$ and the lowest occupied

molecular orbital (LUMO) of spiro-OMeTAD referred to the energy levels of FAPbBr$_3$ and might be enhanced by dipoles formed at the interfaces. A further indication for the high selectivity is given by the fact that the J–V curves for **FA(2)** devices (Figure 2) under illumination and in the dark do not show a pronounced point of intersection.

Biasing the device in forward and collecting the emitted photon flux of electrons and holes that radiatively recombine in the FAPbBr$_3$, we measure an electroluminescence external quantum efficiency (EQE) of ≈10^{-8} ... 10^{-7} for currents of 5–10 mA cm^{-2}. Considering the photovoltaic EQE onset (Figure S5, Supporting Information), we expect a photovoltage of $V_{oc,\ rad} - \Delta V_{oc,\ nonrad.\ loss} = 2.0 - 0.5 = 1.5$ V.[33] This rough estimation is in decent agreement with measured values of V_{oc} close to 1.45 V for this device.

Such a significant improvement in photovoltage was further investigated by impedance spectroscopy (IS). The measurements based on impedance spectroscopy revealed a clear difference in the resistive response of **FA(1)** and **FA(2)** devices. With increasing forward voltage, both the resistances (determined at higher as well as lower frequency range) dropped faster for **FA(1)** device (Figure S6, Supporting Information). Relatively faster nonradiative recombination can explain a lower open-circuit voltage obtained from **FA(1)** devices.[31,34,35]

The reproducibility of our results is ascertained by depicting the photovoltaic efficiency derived from J–V measurements for a batch of 20 devices (Figure S7, Supporting Information). Around 80% of the devices exhibited a photovoltage > 1.4 V under illumination of 100 mW cm^{-2}, further confirming excellent reproducibility of our results. It is worth mentioning that the photovoltage of FAPbBr$_3$ devices remained remarkably stable upon prolonged storage under ambient conditions for more than 3 months (Figure S8, Supporting Information).

Due to the accumulation and migration of ions at various interfaces and within the perovskite solar cells, scan speed dependent hysteresis is observed in current–voltage curves.[36,37] Arguably, hysteresis creates discrepancy in estimating the real photovoltaic parameters obtained from a J–V curve.[38]
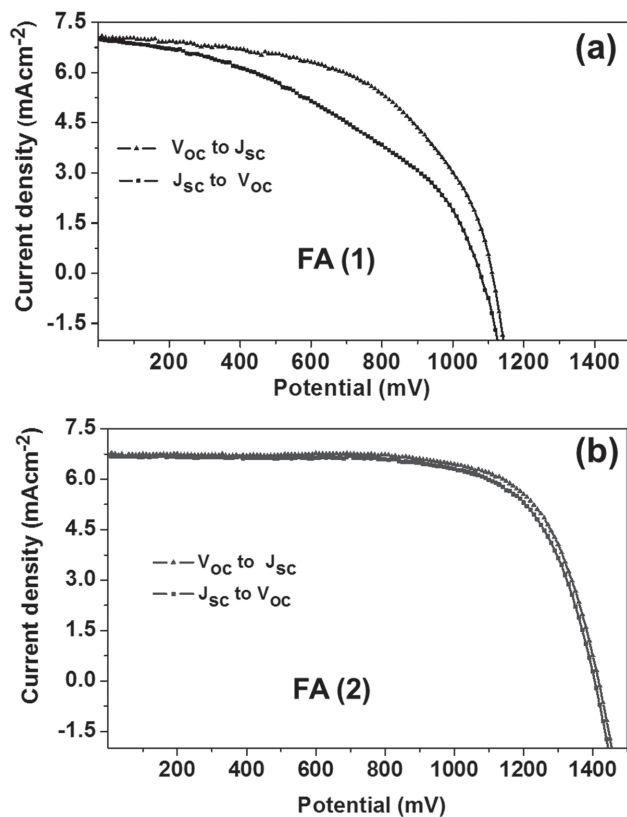
Table 1. Summarized photovoltaic parameters derived from current–voltage curves for the **FA(1)** and **FA(2)** devices fabricated using different precursor solution of PbBr$_2$.

Sample	J_{sc} [mA cm^{-2}]	V_{oc} [V]	FF [%]	PCE [%]
FA(1)	7.1	1.14	67	5.4
FA(2)	6.8	1.42	72	7.0

www.MaterialsViews.com

ADVANCED
FUNCTIONAL
MATERIALS
www.afm-journal.de

FULL PAPER

Figure 4. Current–voltage hysteresis recorded at a scan rate of 0.1 V s^{-1} under stimulated AM1.5 100 mW cm^{-2} photon flux for a) **FA(1)** device and b) **FA(2)** device.

Figure 4a,b shows the hysteresis curves obtained from **FA(1)** and **FA(2)** devices recorded at a scanning rate of 0.1 V s^{-1}. **FA(2)** devices exhibited negligible hysteresis as compared to **FA(1)** devices; in fact the latter displayed a considerable degree of hysteresis. Various strategies have been adopted to fabricate hysteresis-free efficient devices.[13] Surface passivation or minimizing the concentration of vacancies/traps has been surmised as one of the ways to bring down the degree of the hysteresis.[39] Herein, we have achieved so by controlling the growth and formation of FAPbBr$_3$ layer, which further emphasizes the importance of perovskite film formation.

Figure S5 in the Supporting Information shows external quantum efficiency spectra of **FA(1)** and **FA(2)** photovoltaic devices as a function of wavelength. EQE spectra reveal that the generation of photocurrent begins at ≈550 nm, which is in agreement with the band gap of pure FAPbBr$_3$[12] and the current densities obtained from EQE data are in good agreement with J_{sc} values acquired from current–voltage measurements.

2.3. Spectroscopic Studies

2.3.1. Absorption Studies

Comparative analysis of photovoltaic studies of **FA(1)** and **FA(2)** devices showed that the former exhibits slightly higher current density (Figure 2a). Such an enhancement can be attributed to higher loading of FAPbBr$_3$ perovskite in **FA(1)** films as confirmed by cross-sectional SEM analysis. To unravel the difference in short-circuit current densities further; we examined perovskite films with UV–visible absorption spectroscopy in transmission mode. Both **FA(1)** and **FA(2)** films showed a sharp absorption onset around 550 nm (**Figure 5**a) however, **FA(1)** film displayed higher absorbance. Higher absorption indicates relatively higher loading of FAPbBr$_3$ which clearly rationalizes higher current density obtained from **FA(1)** devices.

2.3.2. Photoluminescence Studies

The formation of thicker films which expectedly exhibit higher absorption justifies the generation of higher photocurrent in **FA(1)** devices. To understand the cause of higher V_{oc} in **FA(2)** devices, we performed time-integrated and time-resolved photoluminescence (TRPL) spectroscopy as the V_{oc} in case of optimized contacts is determined by charge carrier dynamics and emission characteristics of the absorber.[40,41]

Figure 5b shows the time-integrated PL spectra acquired at 15 and 300 K for **FA(1)** and **FA(2)** perovskite films. At 300 K, **FA(2)** exhibits stronger PL intensity (>8 times) compared to **FA(1)** sample. As this difference could be due to various reasons, the PL signal is also measured at 15 K, where nonradiative recombination channels are reduced. By comparing the PL intensity at 15 K (inset), which shows comparable values, we surmise that such a contrast in PL intensity at 300 K could arise from variations in the nonradiative recombination rates which are apparently lower in **FA(2)** sample. To gain further understanding of the kinetics of charge carrier decay, we investigated the samples through time-resolved photoluminescence. Figure 5 c,d presents the time-dependent PL decay traces for both **FA(1)** and **FA(2)** films recorded at 300 K. **FA(1)** sample shows a two exponential decay with extremely short decay time components ($\tau_1 = 500$ ps and $\tau_2 = 2$ ns) whereas the **FA(2)** sample exhibits a mono-exponential decay with a relatively long lifetime ($\tau_1 = 24$ ns). From PL and TRPL studies we noticed that the **FA(2)** sample exhibits a lower nonradiative recombination rate and longer lasting charge carriers compared to **FA(1)** which could possibly explain the difference in V_{oc} as shown in Figure 2.[40,41]

2.3.3. Amplified Spontaneous Emission

Amplified spontaneous emission measurements were carried out on **FA(1)** and **FA(2)** films after pumping them with 70 ps laser pulses with tunable wavelengths. ASE was fluently observed in both samples with wide range of pumping wavelengths (430–530 nm). **Figure 6**a,b shows the evolution of emission spectra with increasing pump fluence of 450 nm laser excitation pulses. At low fluence, emission spectrum corresponding to SE centered at ≈550 nm was observed. However over pump fluence threshold, SE is accompanied with the appearance of a sharp peak (transition to ASE) on the lower

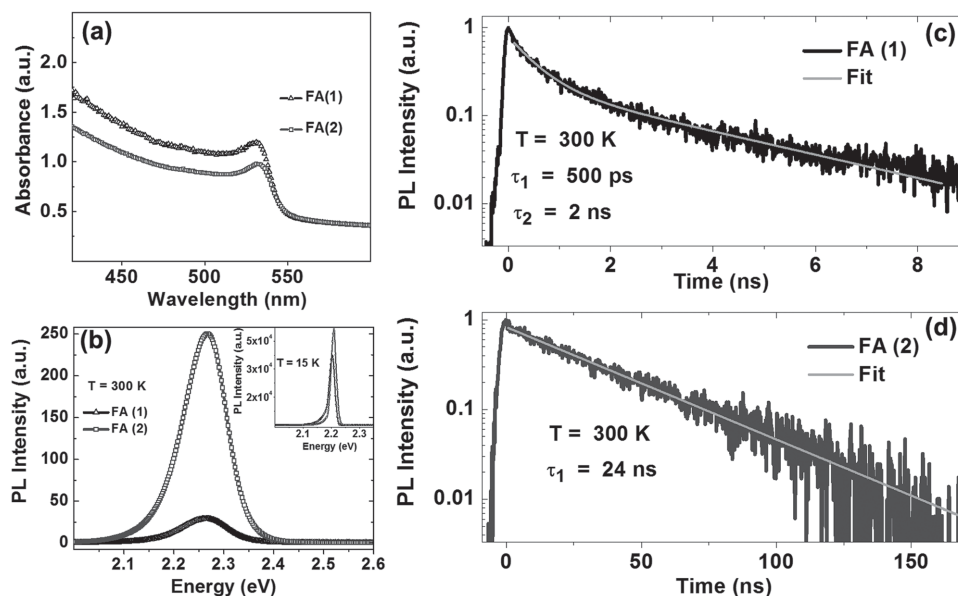**FULL PAPER**

Figure 5. a) UV–visible absorbance spectra of **FA(1)** and **FA(2)** samples. b) Photoluminescence spectra of **FA(1)** and **FA(2)** at 300 K. The inset shows the PL spectra at 15 K. c,d) Decays of PL intensity of **FA(1)** and **FA(2)** at 300 K in semi-logarithmic scale with exponential fitting.

energy side of the broad bands, centered at 557 and 560 nm for **FA(1)** and **FA(2)** samples, respectively.

FA(1) sample displays a slower ASE growth with increasing pump fluence, which makes it more difficult to define the threshold of ASE precisely. Using the two-segment method, ASE threshold of ≈615 µJ cm⁻² was estimated, which corresponds to a threshold carrier density of ≈7.5 × 10¹⁸ cm⁻³. On the other hand, **FA(2)** sample showed a sharp transition from SE to ASE at a pump fluence of 190 µJ cm⁻² per pulse which corresponds to an ASE threshold carrier density of

≈2.3 × 10¹⁸ cm⁻³ (Figure 6c). The absorbance spectrum, thickness and porosity of mp–TiO₂ layer were taken into account for estimating threshold carrier densities. The carrier density values are in agreement with the values reported for MAPbI₃ perovskites, indicating that organic cation contributes marginally to the density of states in organic–inorganic lead halide perovskites.

Furthermore **FA(2)** sample shows a higher quantum efficiency (Figure 6c) (as can be deduced from the sharp slope in the linear region), whereas **FA(1)** sample suffers from a
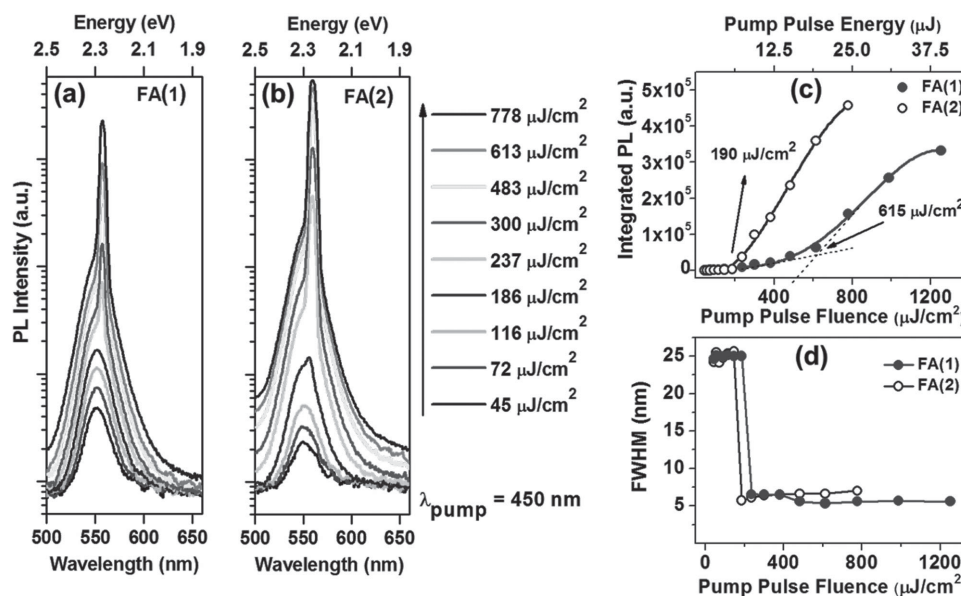

Figure 6. Evaluation of the PL spectra with increasing pump pulse fluence for a) **FA(1)** and b) **FA(2)** film. The y-axes are of the same logarithmic scale for the two figures. c) Integrated PL intensity versus pump fluence for **FA(1)** (solid circles) and **FA(2)** (open circles) films showing, respectively, the ASE threshold at 615 µJ cm⁻²/pulse and 190 µJ cm⁻²/pulse, and d) Evolution of FWHM with increasing pump fluence for **FA(1)** (solid circles) and **FA(2)** (open circles).

reduced quantum efficiency, faster ASE saturation and lesser quantum yield. Such a strong contrast between the two samples clearly illustrates the importance of experimental conditions employed for the synthesis of FAPbBr$_3$ perovskite to achieve desired electro-optical properties. This is not trivial as the realization of high performance in solar cells can be reflected in efficient ASE characteristics as well. Comparatively, **FA(2)** sample displayed better performance most likely because of lower nonradiative recombination rates which are also evident from PL studies. Therefore, we contend that growth and morphology of the perovskite structures considerably influence the nature and type of defects/traps which could affect their optical gain applications.

3. Conclusion

In summary, our work demonstrated the critical role of solvent in controlling the growth of FAPbBr$_3$ perovskite structures. Morphological studies revealed that the surface coverage of the perovskite films remarkably improves when PbBr$_2$ films are deposited from a stoichiometric mixture of DMF and DMSO solvents. To account for these findings, we surmise that besides the enhancement in solubility, employing a mixture of solvents slows down the growth of the lead halide structures during spin coating thus yielding a uniform film with complete surface coverage. The generation of smooth and uniform **FA(2)** films exhibiting stronger emission and longer charge carrier lifetime paved the way for the fabrication of solar cells exhibiting high V_{oc} of 1.42 V and a negligible hysteresis. Arguably, devices based on **FA(2)** FAPbBr$_3$ films perform remarkably better owing to less shunting between TiO$_2$ and spiro-OMeTAD, and reduced nonradiative losses. ASE studies on perovskite films showed that the **FA(2)** films themselves exhibit promising emission characteristics with a sharp transition from SE to ASE and a higher quantum yield along with a high quantum efficiency. Without any contextualization, we believe this work could lead to the fabrication of efficient FAPbBr$_3$-based true green lasers in the future.

4. Experimental Section

Preparation of Photoanode and Device Fabrication: Prior to the deposition of TiO$_2$ compact layer, the FTO substrate was cleaned by ultrasonication in Deconex (0.2% deionized H$_2$O) detergent, rinsed thoroughly with deionized water and ethanol, and then treated in a UV/O$_3$ cleaner for 15 min. A dense TiO$_2$ blocking layer of ≈30 nm thickness was deposited by aerosol spray pyrolysis on a cleaned TCO glass (NSG 10, Nippon sheet glass, Japan) at 450 °C using a commercial titanium diisopropoxide bis(acetylacetonate) solution (75% in 2-propanol, Sigma-Aldrich) diluted in ethanol (1:9, volume ratio) as precursor and oxygen as carrier gas. To form the mesoporous layer, diluted paste (1:3.5 wt. ratio) (Dyesol 30NRD) was spin coated (5000 rpm, acceleration 2000 rpm for 30 s) onto the substrate containing TiO$_2$ compact layer. This was followed by a series of sintering steps (325 °C for 5 min with 15 min ramp time, 375 °C for 5 min with 5 min ramp time, 450 °C for 15 min with 5 min ramp time, and 500 °C for 15 min with 5 min ramp time) in dry air.

Synthesis of CH(NH$_2$)$_2$Br: CH(NH$_2$)$_2$Br was synthesized by dropping slowly 15 mL of hydrobromide acid (48% wt. in water) (Aldrich) into a

solution of 5 g formamidine acetate (Sigma-Aldrich) in methanol cooled at 0 °C. The solution was further stirred for 5 h at room temperature and then at 80 °C for 30 min. The clear solution was concentrated by rotary evaporation at 80 °C until no obvious liquid remained. Subsequently the crude solid was dissolved by a minimum amount of ethanol and reprecipitated in diethyl ether and filtered. The procedure was repeated three times and the resulting white solid was collected and dried at 80 °C under vacuum for 2 days.

Deposition of FAPbBr$_3$ Perovskite: All materials were purchased from Sigma-Aldrich or Acros Organics and were used as received. FAPbBr$_3$ films were deposited using sequential deposition method. 1.2 M PbBr$_2$ precursor solutions were prepared in DMF and DMSO by constant stirring at 60 °C for 30 min. PbBr$_2$ (DMF), PbBr$_2$ (DMF+DMSO in 1:1 volume ratio) and PbBr$_2$ (DMSO) solutions were spin coated onto the mesoporous TiO$_2$ films at 3000 rpm for 30 s. This was followed by annealing the films at 80 °C for 15 min. After cooling to room temperature, the films were dipped into isopropanol solution of FABr (50 × 10^{-3} M) for 5 min at 60 °C, rinsed with 2-propanol for 5 s and dried at 80 °C for 30 min.

Deposition of Hole Conductor and Device Fabrication: To complete the fabrication of devices, spiro-OMeTAD as HTM was deposited by spin coating 40 μL of the prepared solution at 4000 rpm for 30 s. The HTM solution was prepared by dissolving 72.3 mg (2,2',7,7'-tetrakis(*N,N*-di-*p*-methoxyphenylamine)-9,9-spirobifluorene) (spiro-OMeTAD), 17.5 μL of a stock solution of 520 mg mL^{-1} bis(trifluoromethylsulphonyl)imide in acetonitrile, and 29 μL of a stock solution of 300 mg mL^{-1} tris(2-(1H-pyrazol-1-yl)-4-*tert*-butylpyridine)cobalt(III) bis(trifluoromethylsulphonyl)imide in acetonitrile, and 28.8 μL 4-*tert*-butylpyridine in 1 mL chlorobenzene. The device fabrication was carried out under controlled atmospheric conditions with humidity <1%. Finally, device fabrication was completed by thermally evaporating 70 nm of gold layer as a back contact.

Materials and Spectroscopic Characterization: XRD data were collected on a Bruker Advance D8 X-ray diffractometer with a graphite monochromator, using Cu-Kα radiation, at a scanning rate of 0.5° min^{-1}. An FESEM (Merlin) was employed to analyze the morphology of the samples. An electron beam accelerated to 3 kV was used with an in-lens detector. The optical properties of perovskite films were studied using UV–visible absorption and fluorescence spectroscopy. The absorption spectra of perovskite films were recorded with a UV–vis–NIR spectrophotometer (CARY-5) in the transmission mode. To record photoluminescence spectra and PL decay kinetics, the samples were excited by the second harmonic of a picosecond mode-locked Ti:Sapphire laser (80.5 MHz). The excitation beam is focused on the sample by means of a 90 mm focal that allows for an excitation spot diameter of around 100 μm. The average power was kept in the range 1–10 mW, which corresponds to 0.05–0.5 μJ cm^{-2} per pulse. The collected PL was spectrally and temporally analyzed using a 32 cm focal length monochromator equipped with a charge-coupled device (CCD) and a streak camera. Power-dependent PL and ASE studies were carried out using picosecond laser pulses generated using an optical parametric generator (OPG) that is pumped by a Q-switched picosecond Nd:Yag laser with a fundamental output of 1064 nm, pulse duration of 70–80 ps and repetition rate of 15 Hz. The circular laser beam, after passing through the OPG, was focused using a biconvex lens to a diameter of 2 mm.

Device Characterization: The current–voltage characteristics of the perovskite devices were recorded with a digital source meter (Keithley model 2400, USA). A 450 W xenon lamp (Oriel, USA) was used as the light source for photovoltaic (*J–V*) measurements. The spectral output of the lamp was filtered using a Schott K113 Tempax sunlight filter (Präzisions Glas & Optik GmbH, Germany) to reduce the mismatch between the simulated and actual solar spectrum to less than 2%. The photoactive area of 0.16 cm^2 was defined using a dark-colored metal mask. Incident photon-to-current conversion efficiency (IPCE) measurements were made using a 300 W xenon light source (ILC Technology, USA). A double-monochromator spectrometer (Gemini-180, Jobin Yvon Ltd., UK) was used to select and increment the wavelength

of the radiation impinging on the cells. The incident monochromatic light was passed through a chopper running at 1 Hz and the on/off ratio was measured by an operational amplifier. This was superimposed on a white light bias corresponding to an intensity of 10 mW cm^{-2}. IS, electroluminescence and intensity-dependent photovoltage measurements were performed by a Biologic SP300 (BioLogic, France). The measurements were performed with white light light emitting diodes (LEDs) with the intensity of about 1sun. IS measurements were carried out in a frequency range between 7 MHz and 0.05 Hz for potentials between 0 V and about V_{oc} (with a 20 mV sinusoidal AC perturbation) in 50 mV steps. The resulting impedance spectra were analyzed with the ZView software (Scribner Associate).

Supporting Information

Supporting Information is available from the Wiley Online Library or from the author.

Acknowledgements

[1] a) P. Gao, M. Grätzel, M. K. Nazeeruddin, *Energy Environ. Sci.* **2014**, *7*, 2448; b) J.-H. Im, C.-R. Lee, J.-W. Lee, S.-W. Park, N.-G. Park, *Nanoscale* **2011**, *3*, 4088.

[2] D. B. Mitzi, *J. Chem. Soc., Dalton Trans.* **2001**, 1.

[3] A. Kojima, M. Ikegami, K. Teshima, T. Miyasaka, *Chem. Lett.* **2012**, *41*, 397.

[4] a) W. S. Yang, J. H. Noh, N. J. Jeon, Y. C. Kim, S. Ryu, J. Seo, S. I. Seok, *Science* **2015**, *348*, 1234; b) M. Ibrahim Dar, M. Abdi-Jalebi, N. Arora, T. Moehl, M. Grätzel, M. K. Nazeeruddin, *Adv. Mater.* **2015**, *27*, 7221.

[5] J. Luo, J.-H. Im, M. T. Mayer, M. Schreier, M. K. Nazeeruddin, N.-G. Park, S. D. Tilley, H. J. Fan, M. Grätzel, *Science* **2014**, *345*, 1593.

[6] M. Schreier, L. Curvat, F. Giordano, L. Steier, A. Abate, S. M. Zakeeruddin, J. Luo, M. T. Mayer, M. Grätzel, *Nat. Commun.* **2015**, *6*, 7326.

[7] S. Ryu, J. H. Noh, N. J. Jeon, Y. Chan Kim, W. S. Yang, J. Seo, S. I. Seok, *Energy Environ. Sci.* **2014**, *7*, 2614.

[8] G. E. Eperon, S. D. Stranks, C. Menelaou, M. B. Johnston, L. M. Herz, H. J. Snaith, *Energy Environ. Sci.* **2014**, *7*, 982.

[9] A. Kojima, K. Teshima, Y. Shirai, T. Miyasaka, *J. Am. Chem. Soc.* **2009**, *131*, 6050.

[10] E. Edri, S. Kirmayer, D. Cahen, G. Hodes, *J. Phys. Chem. Lett.* **2013**, *4*, 897.

[11] J. H. Heo, D. H. Song, S. H. Im, *Adv. Mater.* **2014**, *26*, 8179.

[12] F. C. Hanusch, E. Wiesenmayer, E. Mankel, A. Binek, P. Angloher, C. Fraunhofer, N. Giesbrecht, J. M. Feckl, W. Jaegermann, D. Johrendt, T. Bein, P. Docampo, *J. Phys. Chem. Lett.* **2014**, *5*, 2791.

[13] N. J. Jeon, J. H. Noh, Y. C. Kim, W. S. Yang, S. Ryu, S. I. Seok, *Nat. Mater.* **2014**, *13*, 897.

[14] R. Sheng, A. Ho-Baillie, S. Huang, S. Chen, X. Wen, X. Hao, M. A. Green, *J. Phys. Chem. C* **2015**, *119*, 3545.

[15] M. F. Aygüler, M. D. Weber, B. M. D. Puscher, D. D. Medina, P. Docampo, R. D. Costa, *J. Phys. Chem. C* **2015**, *119*, 12047.

[16] F. Deschler, M. Price, S. Pathak, L. E. Klintberg, D.-D. Jarausch, R. Higler, S. Hüttner, T. Leijtens, S. D. Stranks, H. J. Snaith, M. Atatüre, R. T. Phillips, R. H. Friend, *J. Phys. Chem. Lett.* **2014**, *5*, 1421.

[17] K. Chen, A. J. Barker, F. L. C. Morgan, J. E. Halpert, J. M. Hodgkiss, *J. Phys. Chem. Lett.* **2015**, *6*, 153.

[18] S. D. Stranks, G. E. Eperon, G. Grancini, C. Menelaou, M. J. P. Alcocer, T. Leijtens, L. M. Herz, A. Petrozza, H. J. Snaith, *Science* **2013**, *342*, 341.

[19] G. Xing, N. Mathews, S. Sun, S. S. Lim, Y. M. Lam, M. Grätzel, S. Mhaisalkar, T. C. Sum, *Science* **2013**, *342*, 344.

[20] M. Saba, M. Cadelano, D. Marongiu, F. Chen, V. Sarritzu, N. Sestu, C. Figus, M. Aresti, R. Piras, A. Geddo Lehmann, C. Cannas, A. Musinu, F. Quochi, A. Mura, G. Bongiovanni, *Nat. Commun.* **2014**, *5*, 5049.

[21] G. Xing, N. Mathews, S. S. Lim, N. Yantara, X. Liu, D. Sabba, M. Grätzel, S. Mhaisalkar, T. C. Sum, *Nat. Mater.* **2014**, *13*, 476.

[22] S. D. Stranks, S. M. Wood, K. Wojciechowski, F. Deschler, M. Saliba, H. Khandelwal, J. B. Patel, S. J. Elston, L. M. Herz, M. B. Johnston, A. P. H. J. Schenning, M. G. Debije, M. K. Riede, S. M. Morris, H. J. Snaith, *Nano Lett.* **2015**, *15*, 4935.

[23] Q. Liao, K. Hu, H. Zhang, X. Wang, J. Yao, H. Fu, *Adv. Mater.* **2015**, *27*, 3405.

[24] G. E. Eperon, V. M. Burlakov, P. Docampo, A. Goriely, H. J. Snaith, *Adv. Funct. Mater.* **2014**, *24*, 151.

[25] a) M. I. Dar, N. Arora, P. Gao, S. Ahmad, M. Grätzel, M. K. Nazeeruddin, *Nano Lett.* **2014**, *14*, 6991. b) M. I. Dar, M. Abdi-Jalebi, N. Arora, M. Grätzel, M. K. Nazeeruddin, *Adv. Energy Mater.* *6*, **2015**, 1501358.

[26] Y. Tidhar, E. Edri, H. Weissman, D. Zohar, G. Hodes, D. Cahen, B. Rybtchinski, S. Kirmayer, *J. Am. Chem. Soc.* **2014**, *136*, 13249.

[27] Y. Wu, A. Islam, X. Yang, C. Qin, J. Liu, K. Zhang, W. Peng, L. Han, *Energy Environ. Sci.* **2014**, *7*, 2934.

[28] a) N. Ahn, D.-Y. Son, I.-H. Jang, S. M. Kang, M. Choi, N.-G. Park, *J. Am. Chem. Soc.* **2015**, *137*, 8696; b) W. Li, J. Fan, J. Li, Y. Mai, L. Wang, *J. Am. Chem. Soc.* **2015**, *137*, 10399.

[29] a) R. Schölin, M. H. Karlsson, S. K. Eriksson, H. Siegbahn, E. M. J. Johansson, H. Rensmo, *J. Phys. Chem. C* **2012**, *116*, 26300; b) W. H. Nguyen, C. D. Bailie, E. L. Unger, M. D. McGehee, *J. Am. Chem. Soc.* **2014**, *136*, 10996.

[30] J. H. Heo, S. H. Im, J. H. Noh, T. N. Mandal, C.-S. Lim, J. A. Chang, Y. H. Lee, H.-j. Kim, A. Sarkar, Md. K. Nazeeruddin, M. Gratzel, S. I. Seok, *Nat. Photon.* **2013**, *7*, 486.

[31] H.-S. Kim, I. Mora-Sero, V. Gonzalez-Pedro, F. Fabregat-Santiago, E. J. Juarez-Perez, N.-G. Park, J. Bisquert, *Nat. Commun.* **2013**, *4*, 2242.

[32] W. Tress, K. Leo, M. Riede, *Appl. Phys. Lett.* **2013**, *102*, 163901.

[33] U. Rau, *Phys. Rev. B* **2007**, *76*, 085303.

[34] A. Dualeh, T. Moehl, N. Tétreault, J. Teuscher, P. Gao, M. K. Nazeeruddin, M. Grätzel, *ACS Nano* **2014**, *8*, 362.

[35] E. J. Juarez-Perez, M. Wußler, F. Fabregat-Santiago, K. Lakus-Wollny, E. Mankel, T. Mayer, W. Jaegermann, I. Mora-Sero, *J. Phys. Chem. Lett.* **2014**, *5*, 680.

[36] W. Tress, N. Marinova, T. Moehl, S. M. Zakeeruddin, M. K. Nazeeruddin, M. Gratzel, *Energy Environ. Sci.* **2015**, *8*, 995.

[37] C. Eames, J. M. Frost, P. R. F. Barnes, B. C. O/'Regan, A. Walsh, M. S. Islam, *Nat. Commun.* **2015**, *6*, 7497.

www.MaterialsViews.com

ADVANCED
FUNCTIONAL
MATERIALS
www.afm-journal.de

FULL PAPER

[38] H. J. Snaith, A. Abate, J. M. Ball, G. E. Eperon, T. Leijtens, N. K. Noel, S. D. Stranks, J. T.-W. Wang, K. Wojciechowski, W. Zhang, *J. Phys. Chem. Lett.* **2014**, *5*, 1511.

[39] Y. Shao, Z. Xiao, C. Bi, Y. Yuan, J. Huang, *Nat. Commun.* **2014**, *5*, 5784.

[40] W. Tress, N. Marinova, O. Inganäs, M. K. Nazeeruddin, S. M. Zakeeruddin, M. Graetzel, *Adv. Energy Mater.* **2015**, *5*, 1400812.

[41] K. Tvingstedt, O. Malinkiewicz, A. Baumann, C. Deibel, H. J. Snaith, V. Dyakonov, H. J. Bolink, *Sci. Rep.* **2014**, *4*, 6071.